VIIRS/SUOMI-NPP Level 2 Cirrus Reflectance (CLDCR_L2_VIIRS_SNPP) Algorithm Theoretical Basis Document

Version 1.2

BO-CAI GAO[1] and RONG-RONG LI

Remote Sensing Division, Naval Research Laboratory
4555 Overlook Avenue, SW, Washington, DC 20375 USA

September 1, 2020

[1]gao@nrl.navy.mil

Revisions

Change record			
Version	**Date**	**Author/changed by**	**Remarks**
0.0	September/2019	Bo-Cai Gao (NRL/DC)	Initial draft
1.0	February/2020	Bo-Cai Gao (NRL/DC)	Change format
1.1	August/2020	Bo-Cai Gao (NRL/DC)	Product name change
1.2	September/2020	Bo-Cai Gao (NRL/DC)	Change descriptions on quality assurance (QA)

TABLE OF CONTENTS

SUMMARY

This algorithm theoretical basis document (ATBD) describes an algorithm for retrieving a cloud (CLD) product, namely the cirrus reflectance (CR) level 2 data product from radiances acquired with the VIIRS (Visible Infrared Imaging Radiometer Suite) instrument on board the Suomi NPP (National Polar-orbiting Partnership) satellite. Hereafter, the product name is abbreviated as 'CLDCR_L2_VIIRS_SNPP'.

VIIRS contains 11 narrow channels (M1 – M11) in the 0.4 – 2.5 μm solar spectral region, in addition to a number of IR emission channels. The M9 channel is specifically designed for detecting thin cirrus clouds. It is centered at 1.378 μm with a width of 15 nm, which is located within a strong atmospheric water vapor band absorption region. In comparison with the corresponding MODIS Channel 26, the VIIRS M9 channel is narrower and significantly more sensitive for cirrus detections. Because the radiances of the M9 channel over cirrus pixels are subjected to absorption by atmospheric water vapor molecules above and within cirrus, the water vapor absorption effect needs to be properly taken into consideration when using the M9 channel for quantitative removal of cirrus effects in other VIIRS channels in the 0.4 – 2.5 μm spectral range. In this ATBD, we describe empirical techniques for the retrieval of cirrus reflectances in the visible and NIR (0.4 – 1.0 μm), where ice particles within cirrus have negligible absorption effects, and shortwave IR (SWIR) (1.0 – 2.5 μm) where ice particle absorption effects are obviously observed. The descriptions include all elements leading to the development of the operational VIIRS L2 cirrus reflectance algorithm, journal literature backing up the approach, theoretical descriptions on algorithm's physics and mathematical background, and sample retrieval results from VIIRS data.

1 INTRODUCTION

This algorithm theoretical basis document (ATBD) describes an algorithm for retrieving a cloud (CLD) product, namely the cirrus reflectance (CR) level 2 data product from radiances acquired with the VIIRS instrument on board the Suomi NPP (National Polar-orbiting Partnership) satellite. Hereafter, the product name is abbreviated as 'CLDCR_L2_VIIRS_SNPP'.

VIIRS contains 11 narrow channels (M1 – M11) in the 0.4 – 2.5 μm solar spectral region, in addition to a number of IR emission channels. The M9 channel is specifically designed for detecting thin cirrus clouds. It is centered at 1.378 μm with a width of 15 nm, which is located within a strong atmospheric water vapor band absorption region. In comparison with the corresponding MODIS Channel 26, the VIIRS M9 channel is narrower and significantly more sensitive for cirrus detections. Because the radiances of the M9 channel over cirrus pixels are subjected to absorption by atmospheric water vapor molecules above and within cirrus, the water vapor absorption effect needs to be properly taken into consideration when using the M9 channel for quantitative removal of cirrus effects in other VIIRS channels in the 0.4 – 2.5 μm spectral range.

In this ATBD, we describe empirical techniques for the retrieval of cirrus reflectances in the visible and NIR (0.4 – 1.0 μm), where ice particles within cirrus have negligible absorption effects, and shortwave IR (SWIR) (1.0 – 2.5 μm) where ice particle absorption effects are obviously observed. The descriptions include all elements leading to the development of the operational VIIRS L2 cirrus reflectance algorithm, journal literature backing up the approach, theoretical descriptions on algorithm's physics and mathematical background, and sample retrieval results from VIIRS data.

2 OVERVIEW AND BACKGROUND INFORMATION

The objectives of this algorithm, the historical perspective on the discovery of the 1.38-micorn channel for remote sensing of cirrus clouds and for the development of cirrus reflectance algorithms, and the special characteristics of the VIIRS M9 cirrus channel, are described in this section.

2.1 Experimental Objective

The purpose of this algorithm is to derive cirrus reflectances in the visible & NIR, and SWIR spectral regions over the globe. The data products can, in principle, be used for improved retrievals of land surface reflectances, water leaving reflectances, and

atmospheric aerosol data products, including optical depths and particle size distributions.

2.2 Historical Perspective

2.2.1 The discovery of the 1.38-μm cirrus detecting channel

Historically, the discovery of the 1.38-μm channel for remote sensing of cirrus clouds didn't come from the traditional atmospheric sciences research community. As early as mid-1960s, researchers already made spectral measurements in the 1.0 – 3.0 μm range above cirrus clouds from aircraft platforms (Blau et al., 1966). These researchers as well as many researchers in the atmospheric sciences community later on were unable to realize the utility of 1.38-μm channels for cirrus detections until the hyperspectral imaging spectrometer data acquired from a high altitude aircraft above cirrus clouds became available in 1990.

The break through came up in early 1990s (Gao et al., 1993) with the analysis of hyperspectral imaging data acquired over cirrus clouds by the NASA JPL AVIRIS (Airborne Visible Infrared Imaging Spectrometer) instrument (Vane et al., 1993; Green et al., 1998) from an ER-2 aircraft at an altitude of ~20 km. The first set of AVIRIS cirrus data was acquired over Rocky Mountains in March of 1990. Around December of 1990, we were able to view the 3-dimensional AVIRIS data (2D spatial and 1-D spectral) set on the newly available Dec 3100 workstation. Specifically, we were able to display different band images sequentially on computer screens. We observed that, cirrus clouds showed up very nicely in images of AVIRIS narrow channels (10 nm wide) located within the strong 1.38-μm water vapor band absorption region and land surface features, such as roads, disappeared in the images. We also observed that, in images of atmospheric 'window' channels centered near 1.24 and 1.5 μm, cirrus cloud features were hardly seen while land surface features were seen obviously. After several days of thinking, we figured out the mechanism for the observation of cirrus and the disappearance of surface features in the 1.38-μm channel images. Because cirrus clouds were high in the atmosphere (~10 km above the sea level or higher), the 1.38-μm solar radiation on the downward sun-surface path was scattered by cirrus and the scattered radiance was then detected by the AVIRIS sensor. The 1.38-μm solar radiation transmitted through cirrus in the downward path was absorbed by water vapor beneath cirrus. As a result, the 1.38-μm channel detected thin cirrus over a nearly 'black' background.

Based on our fresh observation from AVIRIS data and with strong encouragement from NASA scientists and managers, we proposed to fly AVIRIS during the NASA-sponsored FIRE Phase II field experiment conducted over the Gulf of Mexico and Kansas & Oklahoma areas in November and December of 1991. Although NASA HQs managers scheduled two weeks for flying AVIRIS during the 2nd half of the FIRE Phase II experiment, AVIRIS was placed onto ER-2 only for the last three days of the

experiment, and collected data on December 5 and 7. At the time, some members within the FIRE II science team viewed AVIRIS as a 'geological' instrument (due to the fact that AVIRIS was originated from the geology community for mineral mapping purposes, not from the atmospheric community). They insisted on flying their familiar radiometers on ER-2, and left little time for AVIRIS's flights. Nevertheless, AVIRIS collected excellent data sets during the two available flights.

Figure 1 shows examples of AVIRIS images acquired over the Gulf of Mexico measured on December 5, 1991. In the 0.56- and 1.50-μm atmospheric 'window' channel images, both the upper level cirrus clouds and the lower level brighter and isolated cumulus clouds are seen. In the 1.38-μm channel image, only the upper level cirrus clouds are seen. The lower level cumulus clouds disappeared completely because of strong water vapor absorption of solar radiation transmitted through cirrus in the downward sun-surface path. In the 1.35-micorn channel image, weak cumulus cloud features were seen. This is because the atmospheric water vapor absorption effect was not sufficiently strong at this wavelength to result in total absorption of solar radiation beneath cirrus clouds.

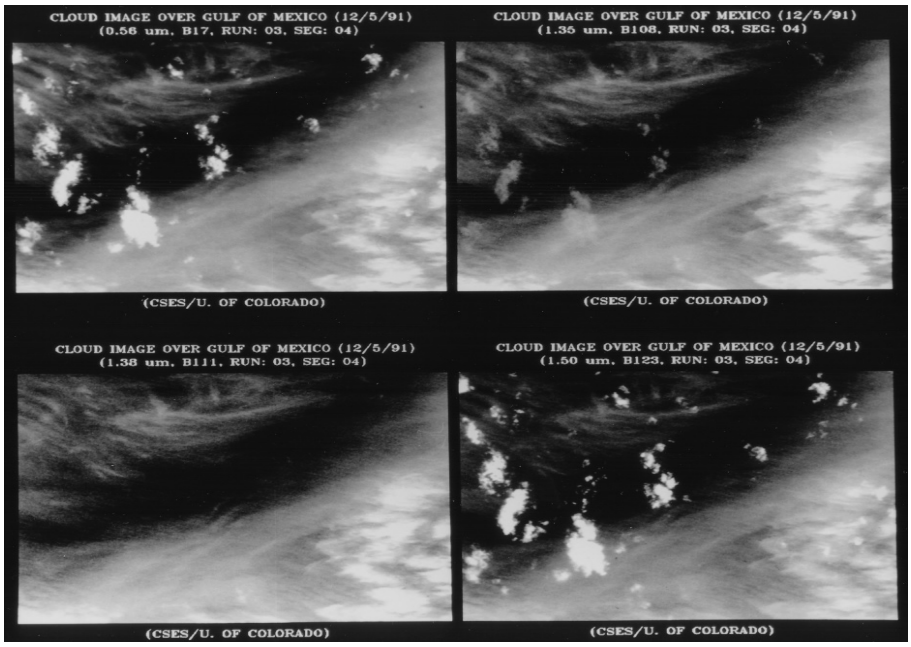

Fig. 1. Examples of AVIRIS images for 10-nm wide channels centered at 0.56, 1.35, 1.38, and 1.50 μm. The images were acquired on December 5, 1992 during the NASA Sponsored FIRE Phase II field experiment over the Gulf of Mexico. The image covers an area of approximately 12 by 10 km^2.

2.2.2 The selection of MODIS Channel 26 (1.38 μm)

During the NASA MODIS Science Team meeting held in December of 1992, we

presented AVIRIS cirrus images. The MODIS Science Team endorsed our idea of putting a narrow channel centered near 1.38 μm (Gao et al., 1995) on MODIS for remote sensing of cirrus clouds. Figure 2 illustrates the position and width of our proposed MODIS cirrus detecting channel, which is centered at 1.375 μm with a width of 30 nm. With strong support from MODIS scientists and management at NASA Goddard Space Flight Center, it was possible to implement this cirrus detecting channel (Band 26) onto MODIS (Salomonson et al., 1989; King et al., 2003) during the very late stage of the MODIS instrument designing.

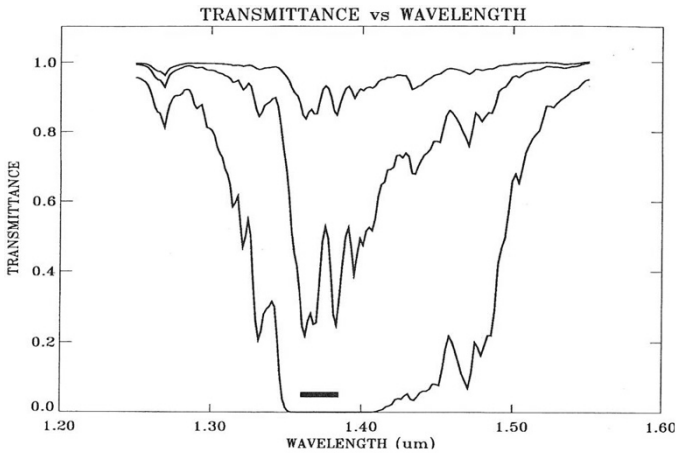

Fig. 2. Illustration of position and width (in thick horizontal bar) of our proposed MODIS 1.38-μm channel for cirrus detections. The three spectral curves are water vapor transmittances for the sun-cloud-sensor ray paths with cloud altitudes at 10, 6, and 0 km (top to bottom) and for a solar zenith angle of 45 degrees, a nadir looking satellite sensor, and a model atmosphere with 2.1 cm of column water vapor amount from the sea level to space.

2.3 The VIIRS Instrument and the M9 Cirrus Detecting Channel

The VIIRS instrument is similar to the Moderate Resolution Imaging Spectroradiometer (MODIS) instruments (Salomonson et al., 1989; King et al., 2003) currently on board the NASA Terra and Aqua Spacecrafts. The VIIRS channel names, positions, and widths are listed in Table 1. Many VIIRS channels (designated as M1 to M16 in Table 1) have heritages to the MODIS instrument but with minor differences in center positions and widths. Important differences between VIIRS and MODIS do exist. For examples, MODIS channels located in atmospheric gaseous absorption regions near 4.5 μm, 6.7 μm, and above 13 μm are all absent in VIIRS. As a result, VIIRS has, in general, less capability for remote sensing of atmospheric temperatures and clouds in comparison with MODIS.

Fortunately, VIIRS has implemented the M9 channel centered at 1.378 μm with a width of 15 nm for remote sensing of cirrus clouds from space. Fig. 3 illustrates the positions and widths of the VIIRS M9 channel and MODIS channel 26. Because the M9 channel is narrower and located in a stronger water vapor absorption region, M9 is more sensitive for thin cirrus detections than MODIS channel 26. The M9 channel detector sensitivity is approximately four times better than that of the corresponding MODIS channel 26 (based on the conversation with VIIRS engineers in the early 2000 time frame). In order to use the M9 channel data for quantitative remote sensing of cirrus clouds and for the correction of thin cirrus effects in other atmospheric window channels, the upper level water vapor absorption effect (as illustrated in Fig. 3) in the M9 channel data needs to be removed. Without accounting for the spatially variable water vapor absorption effects, the VIIRS M9 channel data can only be used qualitatively for cirrus detections, not quantitatively for correcting/removing of cirrus effects in other VIIRS channels.

Table 1: VIIRS channel names, positions, and full widths at half maximum (FWHMs).

VIIRS Channel	λ (μm)	FWHM (μm)
M1	0.412	0.020
M2	0.445	0.018
M3	0.488	0.020
M4	0.555	0.020
M5	0.672	0.020
M6	0.746	0.015
M7	0.865	0.039
M8	1.24	0.020
M9	1.378	0.015
M10	1.610	0.060
M11	2.250	0.050
M12	3.700	0.180
M13	4.050	0.155
M14	8.550	0.300
M15	10.7625	1.000
M16	12.0125	0.950

Soon after the launch of the Suomi VIIRS instrument into space, we evaluated the quality of the M9 channel data. The left plot in Figure 4 shows a VIIRS RGB image acquired over bright desert and dark ocean water areas. Sunglint patterns in the left portion are obviously seen. The right plot in Fig. 4 shows the corresponding VIIRS M9 channel image. Thin cirrus clouds over the bright desert and water surfaces are nicely

detected, while the sunglint features are not seen at all. The Fig. 4 image demonstrated the great capability of the VIIRS M9 channel for cirrus detections over water, land, as well as the areas affected by sunglint.

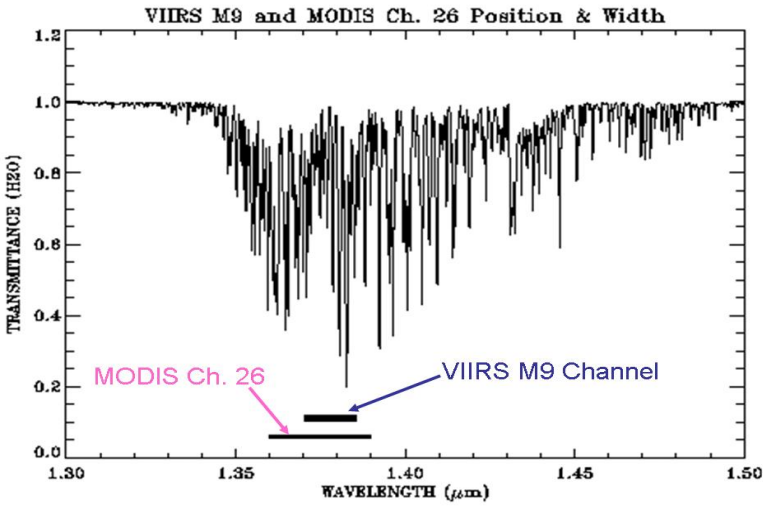

Fig. 3. Positions and widths of VIIRS M9 channel and MODIS channel 26.

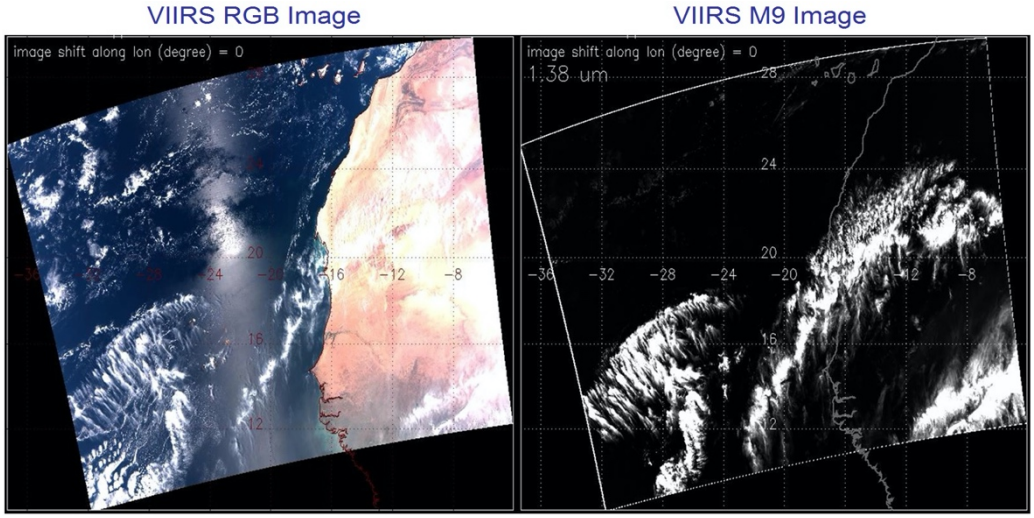

Fig. 4. An example of VIIRS images over desert and sunglint areas.

Figure 5 illustrates our technique for estimating the noise level of VIIRS M9 channel. The left portion shows a section of a VIIRS RGB image strongly affected by sunglint. The middle portion shows the same area of the scene, but for the M9 Channel. The filled 'red square' is an area free of cirrus clouds. We calculated the means and standard deviations for VIIRS M1–M11 channels. The standard deviation for the M9 channel in reflectance unit is 0.00016, which is much smaller than the ocean color

community's requirement of noise level at ~0.001 (in reflectance unit). As a result, the M9 channel image is usable for the removal of thin cirrus scattering effects in other VIIRS channels without introducing noticeable noises into cirrus-corrected images. It should be pointed out that, the horizontal stripes in the RGB image in Fig. 5 are most likely related to the so called 'differential' polarization sensitivities associated with 16 detectors of one channel in the along track direction. To our understanding, the differential polarization issue has not been fully addressed by various VIIRS calibration teams till present.

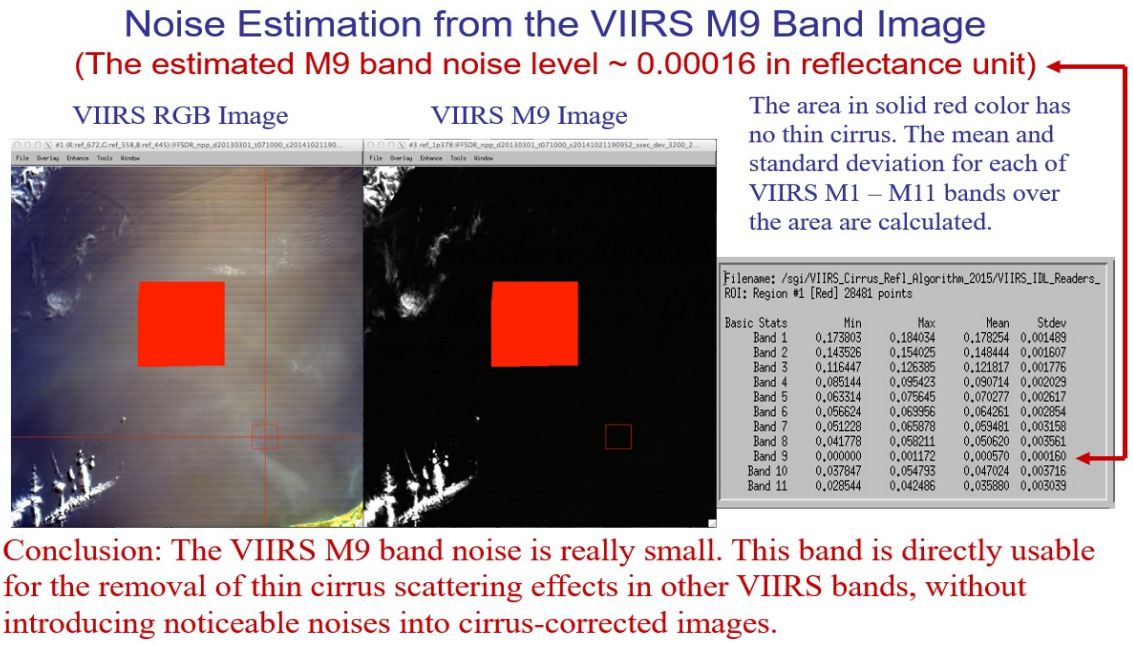

Fig. 5. An illustration on signal to noise estimates for the VIIRS M9 channel.

Due to the great successes in remote sensing of cirrus clouds with AVIRIS, MODIS, and VIIRS using 1.38-μm channels, scientists and engineers have implemented similar 1.38-μm channels with slight differences in center positions and widths onto a number of other satellite instruments, including the DOE's MTI (Multispectral Thermal Imager), Japanese GLI (GLobal Imager), Landsat8 OLI (Operational Land Imager), GOES-R ABI (Advanced Baseline Imager), and European Sentinel 2 MSI (Multi Spectral Instrument). At present, the concept of using a narrow channel centered near 1.38 μm for satellite remote sensing of cirrus clouds has gained worldwide acceptance.

2.4 Previous experiences in developing cirrus reflectance algorithms

Over many years, we have demonstrated the capability of using 1.38-μm cirrus detecting channels for cirrus corrections, and therefore for improved remote sensing of

land surfaces, ocean color, and atmospheric aerosols.

Fig. 6 shows an example of cirrus detection and correction using a MODIS data set acquired over France and Atlantic Ocean. Fig. 6a is an RGB image of the scene. The aircraft induced contrail cirrus clouds contaminate portions of the scene. Fig. 6b is the 1.38-μm channel image of the same scene. The thin contrail cirrus clouds are obvious to see in this image, but the land and ocean surface features are not seen at all, because the solar radiation at this wavelength after transmitting through cirrus clouds in the downward sun-surface path is absorbed by water vapor beneath the cirrus clouds. Fig. 6c shows the cirrus-removed RGB image using the technique described by Gao et al. (2002a). By comparing Fig. 6c with Fig. 6a, it is seen that the land features and water features associated with a coccolithophore blooming event, are seen much better after the cirrus correction.

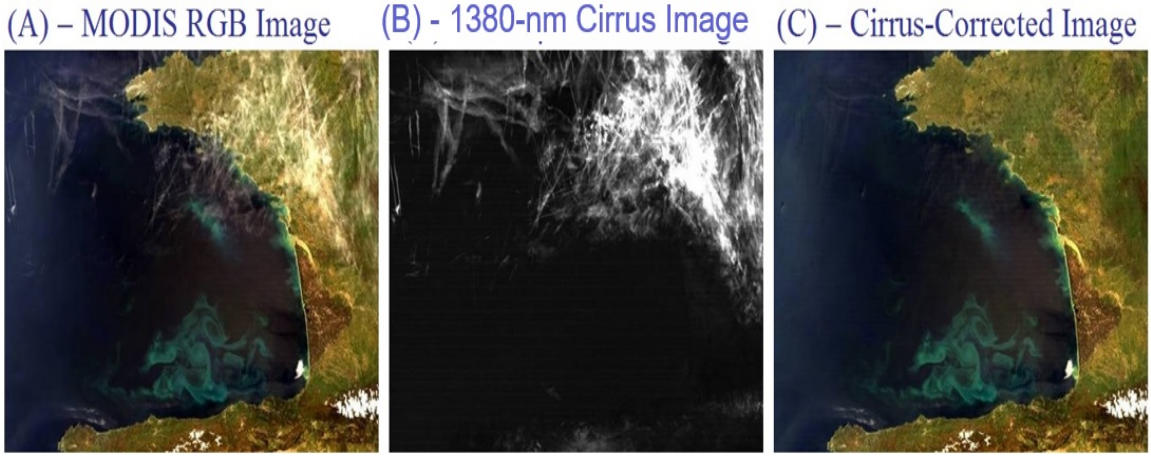

Fig. 6 – An example of cirrus detection and correction over Atlantic Ocean and France.

Another example of cirrus detection and correction is shown in Figure 7. A true color MODIS image (R: 0.645 μm; G: 0.55 μm; B: 0.47 μm) acquired over northeastern part of Canada is shown in Fig. 7a. Land surface features, white cirrus clouds, and blue smoke are seen. The1.38-μm channel image is shown in Fig. 7b. Only the upper level cirrus clouds are seen in this image. Fig. 7c shows an example of correction of thin cirrus effects for three MODIS visible channels using the retrieved cirrus reflectance image (Gao et al., 2002a). By comparing Fig. 7c with Fig. 7a, it is seen that the land surface features and smoke are seen much better after the cirrus correction. Unfortunately, we were unable to convince MODIS aerosol scientists to remove thin cirrus effects from MODIS images prior to making aerosol retrievals from MODIS images in the 0.4 – 2.5 solar spectral range. They only agreed for improved thin cirrus screening using the MODIS Band 26 images (Gao et al., 2002b). At present, within the MODIS aerosol algorithm, pixels with the Band 26 apparent reflectance values greater

than about 0.015 were screened out. The remaining pixels were assumed to be cirrus-free during MODIS aerosol retrievals. As a result, over certain situations, the thin cirrus induced errors in the retrieved aerosol optical depths in the visible from MODIS data can be ~0.1 (even up to 0.2).

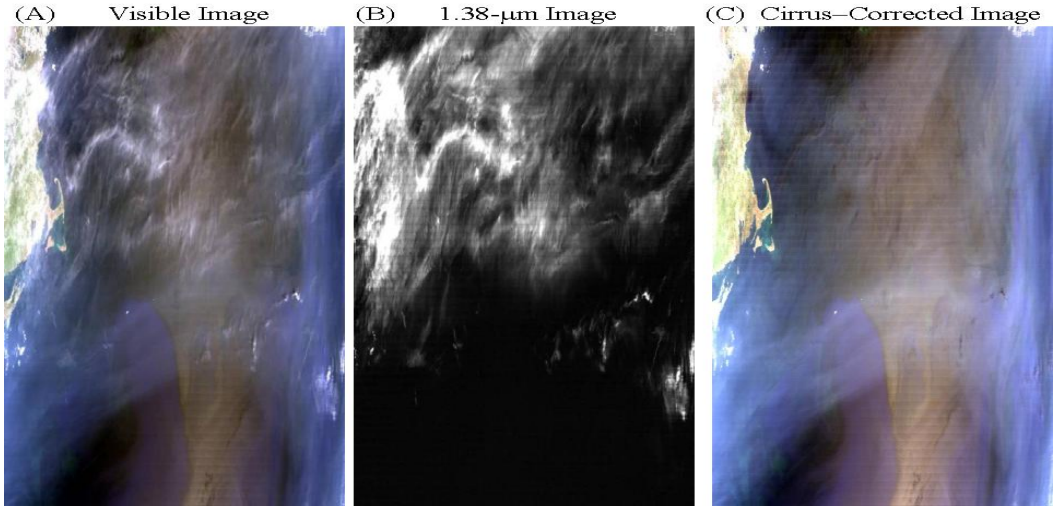

Fig. 7. An example of cirrus detection and correction over North America. The cirrus-corrected image in the right allows better observation of blue smoke and land surface features.

We have multi-year experience in developing cirrus reflectance algorithms. For example, we described a method for correcting thin cirrus path radiances in the 0.4 – 1.0 μm spectral region in AVIRIS data using the 1.375-μm cirrus detecting channel (Gao et al., 1998). Figure 8 shows examples of cirrus detection and corrections with a narrow channel located within the strong water vapor absorption region near 1.38 μm. Fig. 8a is an AVIRIS RGB image acquired over Bowie, Maryland in the summer of 1997. Surface features appear blurred because of the presence of thin cirrus clouds. Fig. 8b is the 1.38-μm channel image of the same scene. Only the upper level thin cirrus clouds are seen. The surface features seen in Fig. 8a disappear completely in Fig. 8b because of absorption of water vapor beneath cirrus. Fig. 8c is the cirrus corrected RGB image. The corrections were made using the method described by Gao et al. (1998). By comparing Fig. 8c with Fig. 8a, it is seen that the surface features are seen much better after the removal of thin cirrus effects.

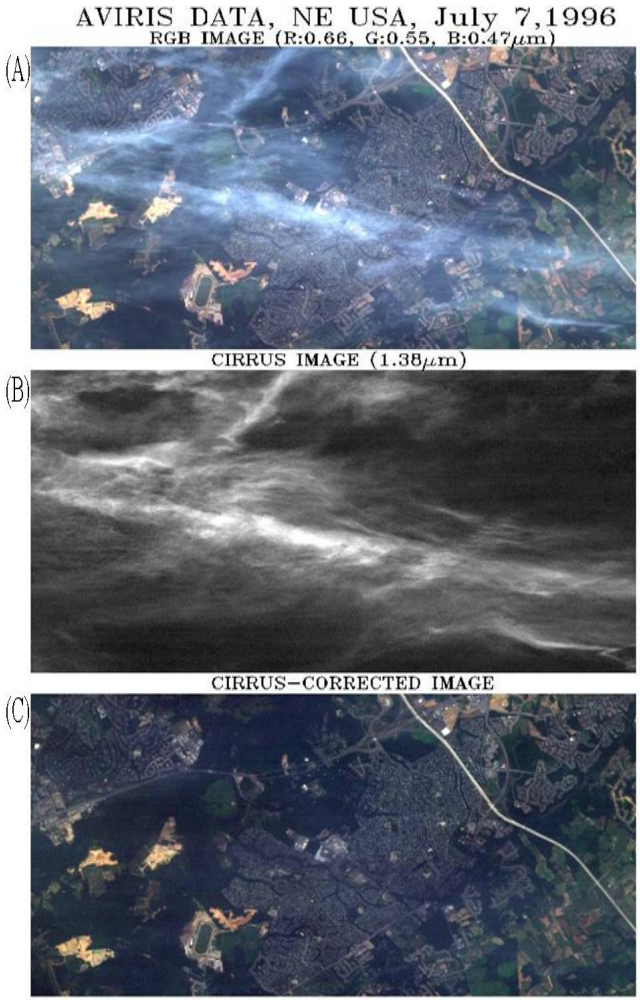

Fig. 8. An AVIRIS RGB image acquired over Bowie, Maryland in the summer of 1997 (a), the 1.38-μm image (b), and the cirrus-corrected RGB image (c).

We developed operational MODIS cirrus reflectance algorithm. A paper on this subject was published in 2002 (Gao et al., 2002a). The daily 'pixel-based' cirrus reflectance product, which is a standard MODIS Level 2 data product, at the 1-km spatial resolution of the MODIS instrument, and the daily, 8-day, and monthly cirrus reflectance products, which are standard MODIS Level 3 products, at a 1° by 1° latitude-longitude grid globally are operationally produced at a NASA computing facility. Figure 9 shows a sample global MODIS L3 image for October, 2002. Large amounts of cirrus clouds are observed in the tropical region as well as over the latitude belt between about 40°S and 60°S in the southern hemisphere. At present, more than 19 years of Terra MODIS and nearly 17 years of Aqua MODIS Level 3 monthly-mean cirrus reflectance data products have been generated. The cirrus reflectance data

products have been used in a variety of climate research and remote sensing applications (e.g., Toth et al., 2013; Turk and Miller, 2005; Jin, 2006, Chen and Liu, 2005).

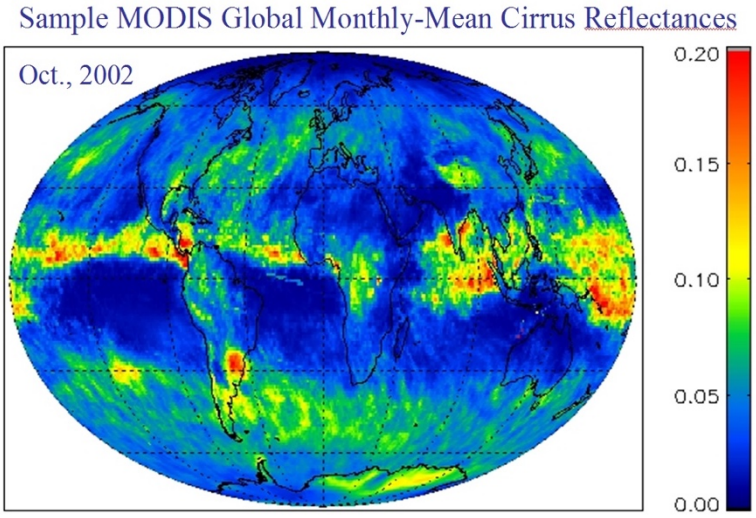

Fig. 9. A sample global MODIS L3 image for Oct. 2002. Large amounts of cirrus clouds are observed in the tropical region as well as over the latitude belts between about 30°S and 60°S.

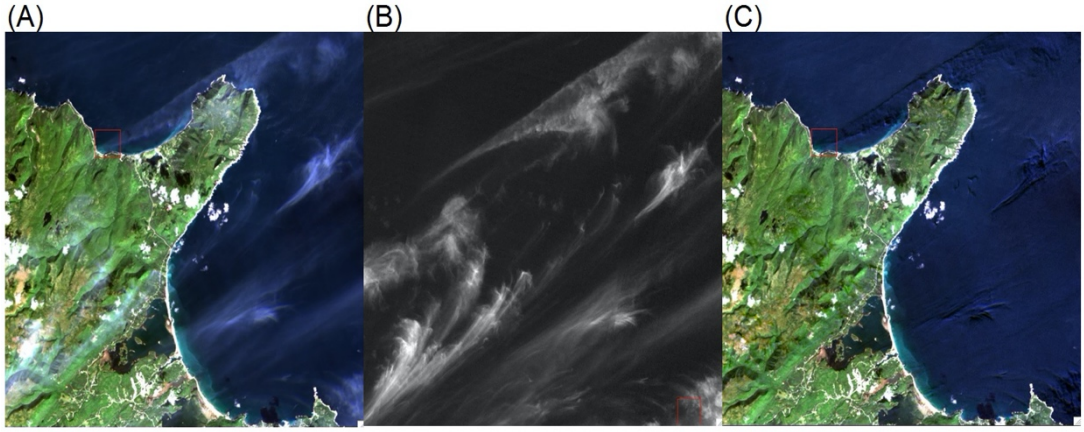

Fig. 10. (A) - A Landsat 8 OLI RGB image acquired over Cape Breton Island in eastern Canada (northeast to Halifax) on September 16, 2014, (B) - the corresponding Band 9 (cirrus band) image, and (C) - the cirrus-corrected RGB image

More recently, we developed a version of cirrus reflectance algorithm (Gao and Li, 2017) suitable for processing Landsat 8 OLI (Operational Land Imager) data. In this version of the algorithm, techniques of retrieving cirrus reflectances for both the

visible/NIR channels and SWIR channels (centered at 1.61 and 2.2 μm), where ice particles within cirrus clouds have absorption effects, are described. Figure 10 shows an example on cirrus detection and corrections with this algorithm. Fig. 10a shows a portion of an OLI true color RGB image. The data was acquired over Cape Breton Island in eastern Canada (northeast of Halifax) on September 16, 2014. Thin cirrus clouds over both land and water surfaces are seen. Fig. 10b shows the OLI Band 9 (1.38-μm) image, where only the upper level thin cirrus clouds are seen. The land and water surface features in Fig. 10a are not seen in Fig. 10b. This demonstrates clearly that the OLI Band 9 is very effective for thin cirrus detection. Fig. 10c shows the resulting cirrus-corrected RGB image. By comparing Fig. 10c with Fig. 10a, it is seen that most cirrus features seen in Fig. 10a are not seen in Fig. 10c, which demonstrates the success of our technique for cirrus corrections of OLI visible bands.

Because Landsat8 OLI has several bands, particularly SWIR bands centered near 1.61 and 2.25 μm, that are very similar to those of the corresponding VIIRS bands, the principles for cirrus reflectance retrievals from Landsat8 OLI and that from VIIRS are about the same. However, the detailed algorithm implementations are different, mainly for dealing with very different spatial coverages between a standard OLI scene (< 200 km by 200 km) and a VIIRS scene (~3000 km by 2000 km).

3 Algorithm Description

The proposed algorithm for retrieving the Level 2 cirrus reflectance data products from VIIRS Level 1b calibrated radiance data is described from both theoretical and practical point of view in this section.

3.1 Theoretical Description

3.1.1 Physics of the problem

Cirrus clouds generally consist of ice particles having different sizes and shapes. The "effective" particle sizes (radii of equivalent spheres) are usually greater than 5 μm. We illustrate the scattering and absorption properties of cirrus clouds through recent hyperspectral imaging data acquired with the AVIRIS-NG instrument from an ER-2 aircraft at an altitude of 20 km. Figure 11 shows a sample AVIRIS-NG spectrum (apparent reflectances) acquired over an area covered by thick cirrus on March 21, 2017. The VIIRS M1 – M11 channel positions and widths are marked in short and thick horizontal bars. In this thick cirrus spectrum, the atmospheric water vapor absorption bands centered near 0.94, 1.14, 1.38, and 1.88 μm are seen. The narrower atmospheric oxygen bands centered near 0.69, 0.76, and 1.26 μm are also seen. In addition, a broad atmospheric ozone absorption band (Chapius band) centered near 0.60 μm. For the

cirrus spectrum, the reflectances of ice particles in the 0.4 – 1.0 μm spectral region are nearly constant with wavelength, because ice particles are much larger than the wavelength and non-absorbing in this spectral region. Past 1.0 μm one finds several ice absorption bands, for example those centered near 1.5 and 2.0 μm. Both the M10 (1.61 μm) and M11 (2.25) channels are affected by ice absorption effects. Because M11 is centered near a local reflectance maximum, the overall ice absorption effect for the M11 channel can be smaller than that of the M10 channel. Weak ice absorptions occur near 1.24 μm (M8) and 1.375 μm (M9); the imaginary parts of the ice refractive index are about the same at both wavelengths. The measured reflectances at 1.375 μm are smaller than those in the 0.4 – 1.0 μm region mainly because of absorption by water vapor above and within the cirrus clouds. These upper-level water vapor absorption effects need to be accounted for in order to use the VIIRS M9 channel for quantitative removal of cirrus effects in M1 – M8 channels. The use of the M9 channel for the removal of M10 and M11 cirrus effects need to take into considerations of the M9 water vapor absorption effects and the M10 and M11 ice absorption and scattering effects.

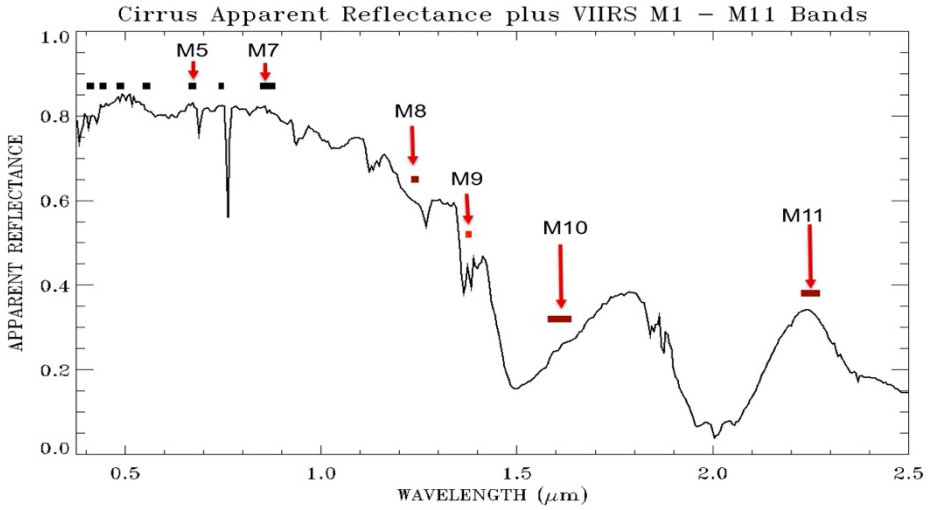

Fig. 11. A thick cirrus apparent reflectance spectrum with VIIRS M1 – M11 channels marked in short and thick horizontal bars.

At present, our knowledge of cirrus ice particle size, shape, and orientation distributions, spatial variability, and scattering phase functions is not sufficient for reliable, routine modeling of cirrus reflectivity (Shiobara and Asano, 1994). Cirrus spatial inhomogeneity and adjacency effects (contamination of one pixel by photons scattered from neighboring pixels) are poorly treated in radiative transfer models. In view of these difficulties, we decided to use empirical relationships to characterize the main cirrus properties, and from these to develop an empirical cirrus removal technique.

3.1.2 Mathematical description of the algorithm

Cirrus clouds are typically located at the upper portion of the troposphere and the lower end of the tropopause. As far as atmospheric scattering effect is concerned, we can assume that a homogeneous thin cirrus layer is located above a "virtual surface", which includes the effects of scattering by molecules, aerosols, and low clouds as well as land or ocean surface reflection and sub-surface scattering. Omitting for convenience the wavelength (λ) and cosine-solar-zenith-angle (μ_0) dependencies, we denote the "apparent reflectance" at the satellite as

$$\rho^* = (\pi L / \mu_0 E_0), \quad (1)$$

where L is the radiance measured by the satellite and E_0 is the extra-terrestrial solar flux.

As described above, the solar radiance within the VIIRS M9 cirrus band is partially absorbed by water vapor molecules located above and within cirrus clouds (see Fig. 11). It is practically difficult to derive quantitatively both the upper level water vapor transmittance factor and the cirrus reflectance on a pixel-by-pixel basis from the one-band (M9) 1.375-μm cirrus image, i.e., it is not possible to retrieve two unknowns from one measurement. In view of this situation, we have decided to obtain the correlation between a given band image and the 1.375-μm cirrus image (Gao et al., 1998; Gao et al., 2002a). We then use the correlation and the 1.375-μm cirrus image to obtain the cirrus reflectance image of a given band. In this way, *the information contained in the spatial domain of a scene is used for the derivation of a mean value of upper level water vapor transmittances of a scene.* Below we use two AVIRIS data sets, one acquired over dark ocean waters where there were no bottom reflection contributions and the other over the land/water boundary areas where the bottom surface reflection effects were not negligible, to illustrate our empirical technique for the retrieval of cirrus reflectances on a pixel-by-pixel basis within small imaging areas (~12 km by 10 km).

A Dark Ocean Scene

Figure 12a is the 0.86-μm AVIRIS image acquired over Monterey Bay, California, in September of 1992. Fig. 12b is a scatter plot of ρ^*(1.38 μm) versus ρ^*(0.86 μm) for all pixels in the scene. The data points are approximately linearly related with a slope ($S_{0.86}$) of 0.65. Here, $S_{0.86}$ is essentially the 1.38-μm band's water vapor transmittance factor. The small offset, ρ_R(0.86 μm), in the horizontal axis is due to weak atmospheric Rayleigh scattering effect at the 0.86-μm band. The Rayleigh scattering effect at the 1.38-μm band is practically negligible. Because the water leaving reflectance contributions at 0.86 μm

for the water scene is zero, $\rho^*(0.86\ \mu m)$ for the atmospheric window band is equal to the sum of $\rho_R(0.86\ \mu m)$ and the cirrus reflectance $\rho_C(0.86\ \mu m)$, i.e.,

$$\rho^*(0.86\ \mu m) = \rho_C(0.86\ \mu m) + \rho_R(0.86\ \mu m) \quad (2)$$

In view of the scatter plot in Fig. 12b, we have

$$\rho^*(1.38\ \mu m) = S_{0.86}\ (\rho^*(0.86\ \mu m) - \rho_R(0.86\ \mu m))$$
$$= S_{0.86}\ \rho_C(0.86\ \mu m), \quad (3)$$

and $\rho_C(0.86\ \mu m)$ can be obtained from $\rho^*(1.38\ \mu m)$ provided that the slope, $S_{0.86}$, is estimated from this scatter plot with, for example, the technique described by Gao et al. (2002a). The derivation of the factor $S_{0.86}$ this way makes use of both the spectral information (the 0.86-μm band and the 1.38-μm band within a pixel) and the spatial information (all pixels in the Fig. 12a image). It should be pointed out that only one value of $S_{0.86}$ per scene is derived, and $S_{0.86}$ is not a pixel-by-pixel quantity. Solving Eq. 3 for $\rho_C(0.86\ \mu m)$, we obtain:

$$\rho_C(0.86\ \mu m) = \rho^*(1.38\ \mu m) / S_{0.86} \quad (4)$$

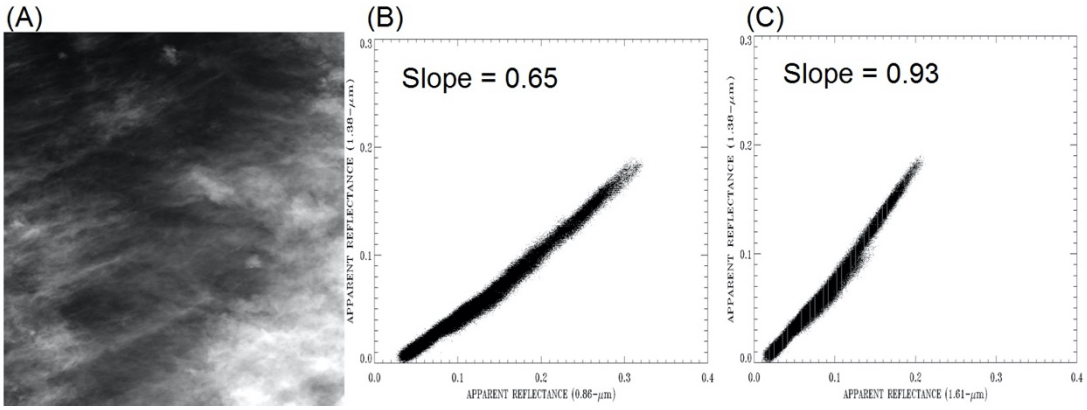

Fig. 12. (A) - An AVIRIS 0.86-μm band image acquired over water surfaces, (B) - scatter plot of 1.38-μm band apparent reflectance image versus the 0.86-μm band image, and (C) - scatter plot of 1.38-μm band apparent reflectance image versus the 1.61-μm band image.

Fig. 12c is similar to Fig. 12b, except that the scatter plot is for $\rho^*(1.38\ \mu m)$ versus $\rho^*(1.61\ \mu m)$. The data points in Fig. 12c are approximately linearly related with a slope ($S_{1.61}$) of 0.93. The slope value $S_{1.61}$ is larger than that of $S_{0.86}$ mainly because the 1.61-μm band is less reflecting and ice has absorption effect at the wavelength (see Fig. 11). With similar reasoning described above, we have

$$\rho^*(1.38\ \mu m) = S_{1.61}\ \rho_C(1.61\ \mu m), \quad (5)$$

or equivalently,

$$\rho_C(1.61\ \mu m) = \rho^*(1.38\ \mu m) / S_{1.61}. \quad (6)$$

$\rho_C(1.61\ \mu m)$ can be obtained from $\rho^*(1.38\ \mu m)$ if the slope, $S_{1.61}$, is estimated from the Fig. 12c scatter plot. The main point we try to make here is that both the 0.86-µm and the 1.61-µm cirrus reflectances are linearly related to the 1.375-µm "apparent reflectances". After deriving $S_{0.86}$ and $S_{1.61}$ from the scatter plots, we can calculate the 0.86-µm and the 1.61-µm band cirrus reflectances using Eq. 4 and 6, respectively.

A Mixed Ocean and Land Scene

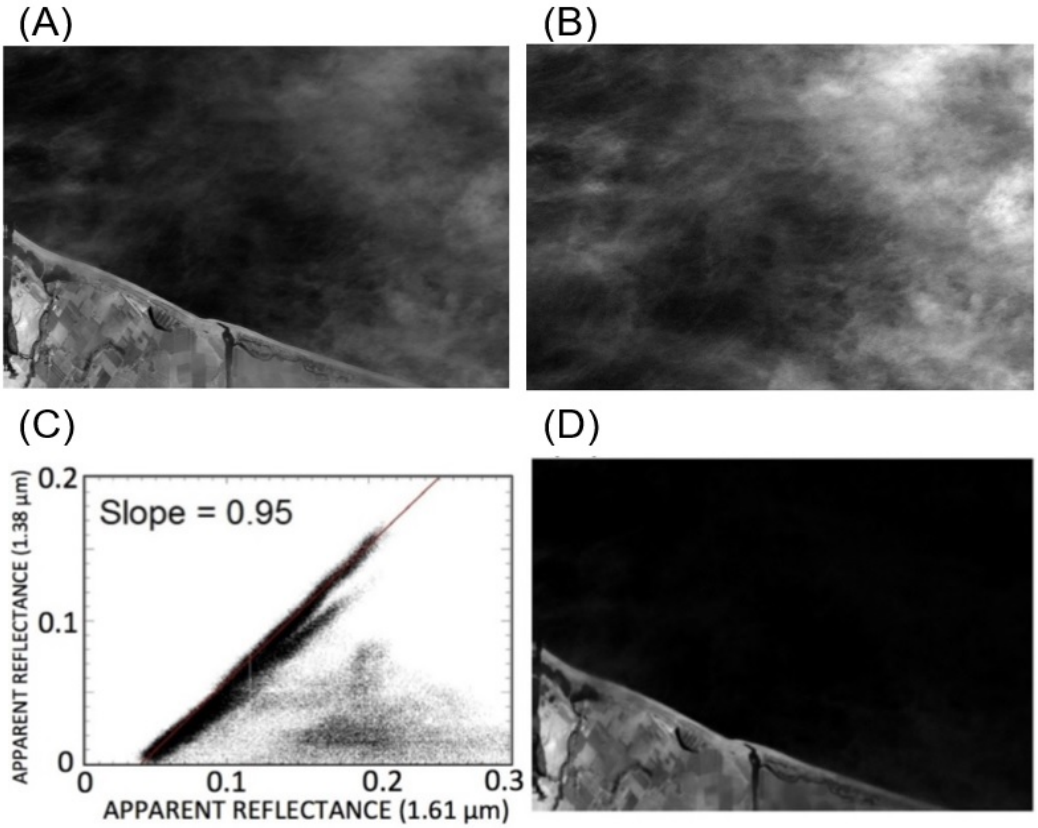

Fig. 13. (A) - An AVIRIS 1.61-μm band image acquired over land and water surfaces, (B) - the 1.38-μm cirrus band image, (C) - scatter plot of 1.38-μm band apparent reflectance image versus the 1.61-μm band image, and (D) - cirrus effect removed 1.61-μm band image.

Figure 13a is the 1.61-μm image of another AVIRIS scene acquired over Monterey Bay, California on September 4, 1992. It covered both land and water surfaces. Fig. 13b

is the 1.38-μm image of the same scene. Only the upper level cirrus clouds are visible. Fig. 13c is the scatter plot of ρ^*(1.38 μm) versus ρ^*(1.61 μm) for all pixels in the scene. Dark surface pixels affected by cirrus clouds are clustered on the left side along a straight line of the scatter plot. The brighter surface pixels affected by cirrus are located in the lower right portion of the scatter plot. Using a numerical procedure, such as the one described by Gao et al. (2002a), a slope ($S_{1.61}$) value of 0.95 with an error of approximately 2% was derived. Only those pixels located on the left edge portions of the scatter plot were used in the estimation of $S_{1.61}$. The bright pixels affected by surface reflection in the 1.61-μm image were automatically excluded during the fitting process. The cirrus introduced reflectances, ρ_C(1.61 μm), to the 1.61-μm band image are equal to ρ^*(1.38 μm) / $S_{1.61}$. Fig. 13d is the cirrus-corrected 1.61-μm image (ρ^*(1.61 μm) – ρ^*(1.38 μm) / $S_{1.61}$). The obvious cirrus features seen in Fig. 13a are not present in Fig. 13d, which demonstrates that the thin cirrus scattering effects are properly removed. It should be pointed out that, if a scene does not contain waters, the darker 1.61-μm pixels with varying cirrus contaminations will also cluster around a straight line in the left side of scatter plot of ρ^*(1.38 μm) versus ρ^*(1.61 μm) band image (see Fig. 13c), and the slope $S_{1.61}$ can still be derived from the scatter plot.

3.1.3 A summary on the empirical cirrus correction procedures

We have provided specific examples to illustrate cirrus reflectance properties, correlations between bands, and cirrus corrections. Below is a summary of the procedures for removing cirrus scattering effects of a given band (B) using the information contained in the 1.38-μm (cirrus band):

a) converting the measured radiances (L) into apparent reflectances (ρ^*) using Eq. (1);
b) making the scatter plot of ρ^*(cirrus) versus $\rho^*(B)$ (e.g., Fig. 13c);
c) estimating the slope, S_B, from the scatter plot (also see Fig. 13c);
d) calculating the cirrus reflectance of the given band, $\rho_C(B)$, which is equal to $\rho^*(\text{cirrus})/S_B$;
e) subtracting out the cirrus reflectance, $\rho_C(B)$, from the measured apparent reflectance, $\rho^*(B)$, for removing the cirrus scattering effect in band B.

It should be pointed out that the procedures described above are applicable for correction of cirrus scattering effects of any given band in the 0.4 – 2.5 μm solar spectral range, regardless whether the band has ice absorption effect or not. Our previously reported techniques (Gao et al., 1998; Gao et al., 2002a) were mainly for the removal of

cirrus scattering effects for bands located in the 0.4 – 1.0 μm where the ice particle absorption effect is negligible.

3.1.4 Algorithm implementations

The examples of cirrus corrections presented in Fig. 12 and 13 are for two scenes covering small areas with the cross-track sizes of approximately 12 km. For such small areas, the upper level water vapor within and above cirrus clouds can be considered to be spatially homogeneous. One mean slope value for a scene is good enough for cirrus correction of a given band.

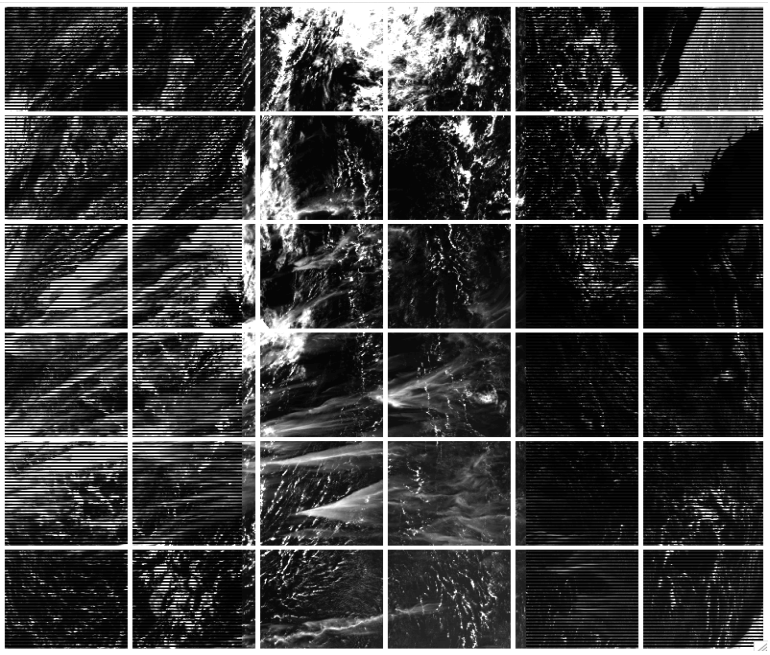

Fig. 14. A VIIRS M5 (0.66-μm) image acquired on July 10, 2017 at UTC 0936. The complete scene is divided into 6 by 6 smaller sub-scenes during the cirrus reflectance retrieving process.

However, the spatial area covered by a standard VIIRS 6-minute granule is typically more than 3000 x 2000 km^2. Over such a large scene, we can no longer assume that the upper level water vapor distributions are spatially homogeneous. To overcome this inhomogeneous problem, we typically divide a whole VIIRS scene into 6 by 6 smaller sub-scenes. Figure 14 shows an example of VIIRS M5 (0.66-μm) channel image (acquired on July 10, 2017 at UTC 0936), where the complete scene is divided into 36 smaller scenes. For each sub-scene, we use the scatter plot approach, as illustrated in Fig. 12c, to derive a mean slope value for a given VIIRS VIS-NIR band, or a SWIR band. Using 2-dimensional linear interpolation and extrapolation techniques (Gao et al.,

2002a), we then obtain slope values (S_B) of a given band for the entire scene on the pixel-by-pixel basis from the 36 mean slope values. The pixel-by-pixel based cirrus reflectances, $\rho_C(B)$, are finally obtained through the equation

$$\rho_C(B) = \rho^*(\text{M9}) / \ S_{B,} \tag{7}$$

where $\rho^*(\text{M9})$ is the apparent reflectances of the VIIRS M9 band. To make cirrus correction, we subtract out the cirrus reflectance, $\rho_C(B)$, from the measured apparent reflectance, $\rho^*(B)$. The resulting cirrus-corrected apparent reflectance for band B, $\rho^*(B\_Corr)$, is obtained according to the following equation:

$$\begin{aligned} \rho^*(B\_Corr) &= \rho^*(B) - \ \rho_C(B) \\ &= \rho^*(\text{B}) - \rho^*(\text{M9}) / S_{B.} \end{aligned} \tag{8}$$

Below we use specific VIIRS case studies to further illustrate the cirrus reflectance derivation and the subsequent cirrus correction processes. Figure 15a is the M5 apparent reflectance image for the 5th row and 4th column sub-scene of Fig. 14. Thin cirrus clouds and lower level brighter water clouds are seen. Fig. 15b is the corresponding M9 apparent reflectance image. Only the upper level cirrus clouds are seen. Fig. 15c is the scatter plot of apparent reflectance images of M9 versus M5 bands. Pixels with least surface and lower level water cloud reflection contributions are located near the left edge portion of the scatter plot. These pixels are used for the estimation of the slope (shown in a short red line in the plot). During the slope estimation process, bad pixels with negative reflectance values or fill values are first eliminated. Very bright pixels with M5 apparent reflectance values greater than 1.0 are also eliminated. The data points along the vertical axis (M9 apparent reflectance) are divided into 20 layers. For each of the layers, the data points are sorted according to the apparent reflectance values of the M5 band from low to high. In order to eliminate possible additional noisy and bad pixels, 5% of pixels in the lower end of M5 band apparent reflectance values are rejected. The next 5% of the pixels are used to calculate mean values of apparent reflectances for the M5 and M9 bands for a given layer. For the 20 layers, we have a total of 20 pairs of mean M5 and M9 apparent reflectances. The 20 data pairs are then used for the estimation of a mean slope value, as illustrated in the thick red line in Fig. 15c. Fig. 15d is the retrieved M5 band cirrus reflectance image (see Step d above), which is brighter than the Fig. 15b M9 apparent reflectance image. This is because the estimated slope value is smaller than 1.0, and the division of the M9 image by the slope value increased the M5 band cirrus reflectance value. In order to test if the estimated M5 cirrus reflectances are correct, we show in Fig. 15e the cirrus corrected M9 band apparent reflectance image. By comparing Fig. 15e with Fig. 15a, it is seen that cirrus

cloud features are properly removed in the Fig. 15e image. This demonstrates that the derived M5 band cirrus reflectances are sufficiently accurate for pixel-by-pixel cirrus removals.

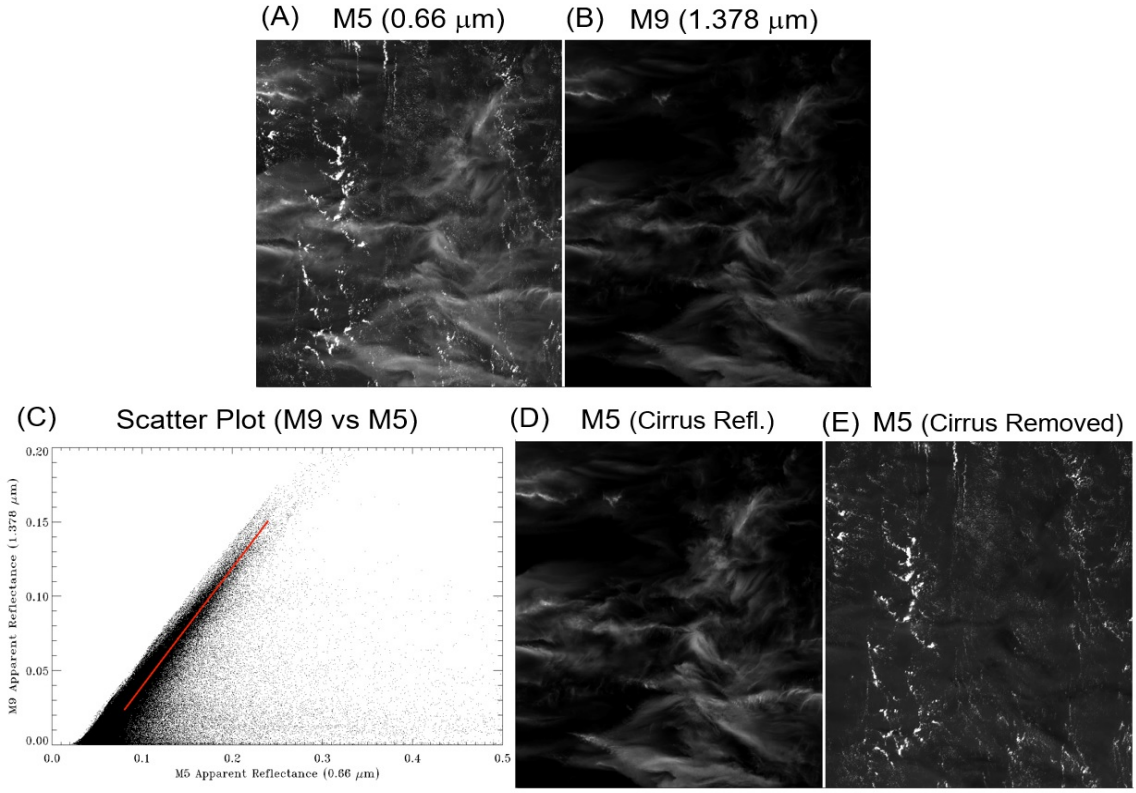

Fig. 15. (A) – A portion of a VIIRS M5 band apparent reflectance image, (B) – the M9 band apparent reflectance image, (C) – scatter plot of M9 versus M5 band images, (D) – the derived M5 band cirrus reflectance image, and (E) – the cirrus-removed M5 band apparent reflectance image.

Figure 16 is similar to Fig. 15, except for the illustration of cirrus reflectance derivations and cirrus corrections for the VIIRS M11 (2.25 μm) band. For consistency, all the images in Fig. 15 and Fig. 16 are processed in the same way. Pixels with apparent reflectance values smaller than zero are assigned a value of zero. Pixels with apparent reflectance values greater than 0.4 are mapped with a value of 255. Pixels with reflectance values between 0 and 0.4 are linearly mapped to values between 0 and 255. As a result, the brightnesses of images in both Fig. 15 and 16 can be compared directly. For examples, the Fig. 16a image is darker than the Fig. 15a image. This is because ice clouds and water clouds have more absorption effects near 2.25 μm than those near 0.66 μm. The data points in the Fig. 16c M9 versus M11 band scatter plot are pushed towards the left side than those in the Fig. 15c scatter plot because the M11 apparent reflectances are smaller than those of M5 apparent reflectances. By comparing Fig. 16e

with Fig. 16a, it is seen that cirrus cloud features are properly removed in the Fig. 16e image. This demonstrates that the derived M11 cirrus reflectances (Fig. 16d) are suited for pixel-by-pixel cirrus removals for the M11 SWIR band that is affected by ice particle absorption.

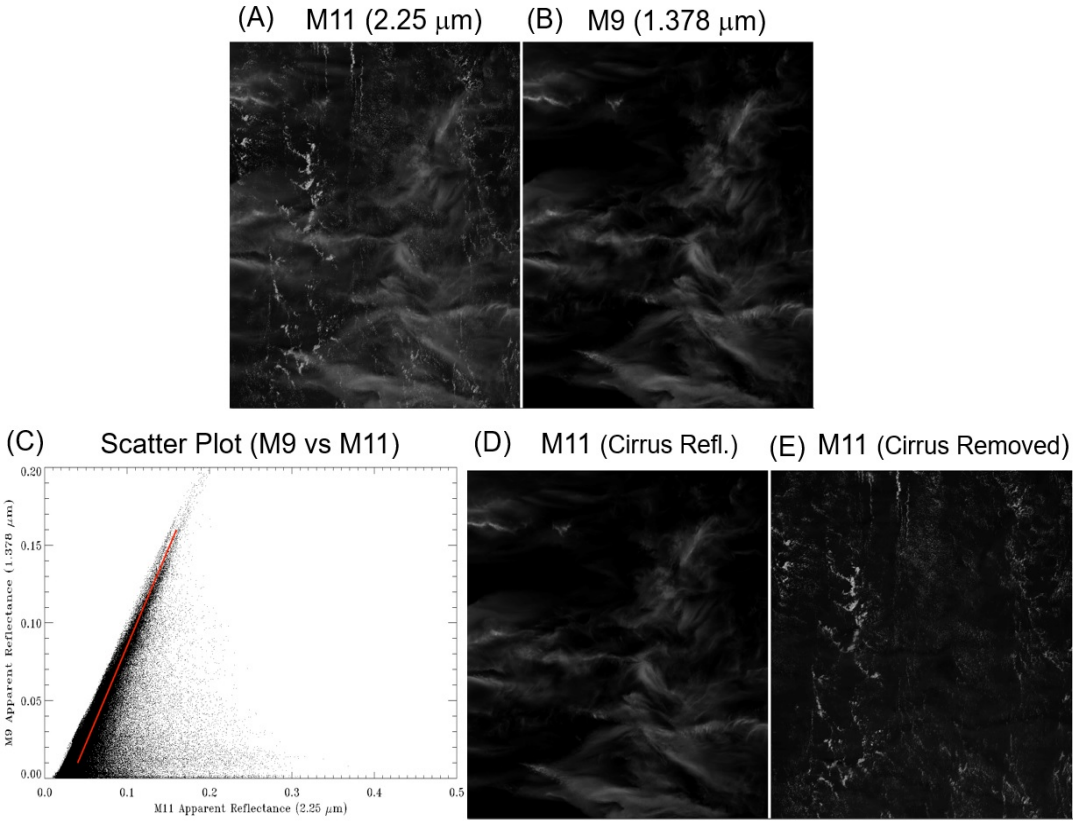

Fig. 16. (A) – A portion of a VIIRS M11 band apparent reflectance image, (B) – the M9 band apparent reflectance image, (C) – scatter plot of M9 versus M11 band images, (D) – the derived M11 band cirrus reflectance image, and (E) – the cirrus-removed M11 band apparent reflectance image.

It should be pointed out that, for certain sub-divided VIIRS imaging blocks (as illustrated in Fig. 14 for imaging sub-division), it is not possible to obtain reliable slopes from the scatter plots. For example, for an imaging block that does not contain any cirrus clouds at all, the M9 band apparent reflectance values are all close to zero, and it is not possible to get a stable estimate of the slope from the scatter plot of M9 band versus any of the other VIIRS M-series of bands. Under the circumstances, we need to assign default slope values for the imaging blocks. In view of this situation, we have developed a routine, which takes account of bandpasses of both VIIRS M9 and MODIS Ch. 26. We calculated the Sun-cirrus-VIIRS ray path M9 transmittance as a function of

{1/cos(solar zenith angle) + 1/cos(view zenith angle)} for discrete sets of solar angles and view angles using an atmospheric transmittance algorithm. The result is shown as the solid line in Fig. 17. For comparison, the corresponding curve for MODIS Ch. 26 is also shown in Fig. 17 (the dotted line). Using a nonlinear least squares fitting routine, we obtained a nonlinear and analytical form of VIIRS M9 transmittance as a function of {1/cos(solar zenith angle) + 1/cos(view zenith angle)} with two parameters. The factors inside the bracket {} are related to the geometric factors for the downward Sun-cirrus ray path and the upward cirrus-VIIRS sensor path. The nonlinear function has been incorporated into our VIIRS cirrus reflectance algorithm.

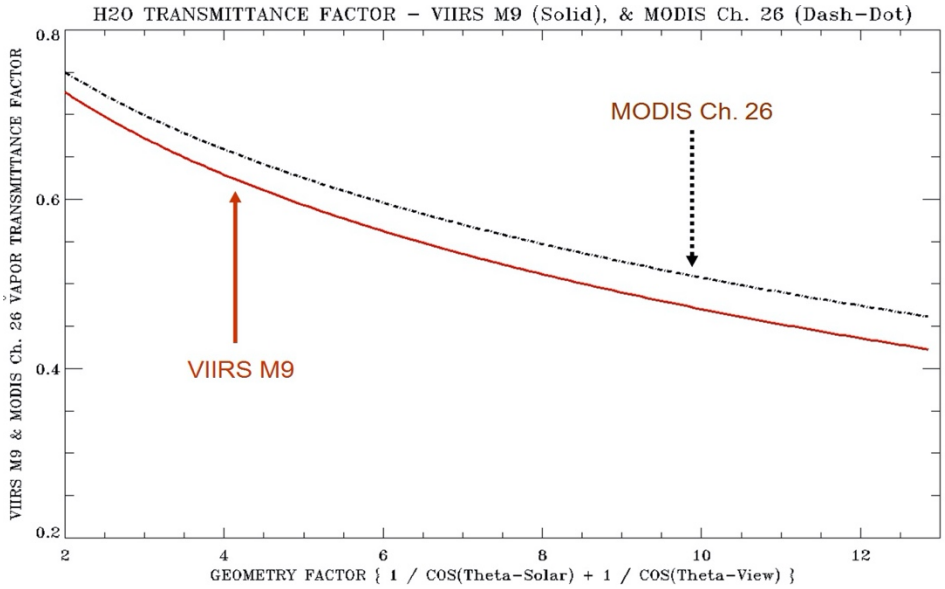

Fig. 17. Simulated VIIRS M9 and MODIS Ch. 26 in the Sun-cirrus-sensor ray path as a function of {1 / (cos(solar zenith angle) + 1/cos(view zenith angle)}.

3.1.5 Quality assurance

Under typical atmospheric conditions with column amount of atmospheric water vapor at 0.4 cm or larger, there is sufficient amount of water vapor in the lower level of the atmosphere to cause total absorption of solar radiation near 1.38 μm in the sun-surface-sensor ray path. The VIIRS M9 channel detects the solar radiation scattered by the upper level cirrus clouds without contaminations from the bottom surfaces. However, under very dry atmospheric conditions with column amount of water vapor at 0.1 to 0.2 cm, the M9 channel also receives solar radiation reflected and scattered by the earth's surfaces. Figure 18a shows a portion of a VIIRS RGB image acquired over the high elevation Tibet Plateau during a dry season. Clouds and surface features are observed. Fig. 18b shows the corresponding M9 channel image. It is obvious to see that

weak land features over clear surface areas are present in this image. Fig. 18c is a QA (Quality Assurance) image we generated based on a variety of criteria (to be described in details below) applied to the VIIRS data set. In this QA image, pixels with poor qualities are assigned a value of zero. Pixels with high qualities are assigned a value of 2. The remaining pixels are assigned a QA value of 1. Fig. 18d is the M9 image after application of a mask based on QA values of the pixels in the scene. By comparing Fig. 18d with Fig. 18b, it is seen that most land features are successively masked out in Fig. 18d.

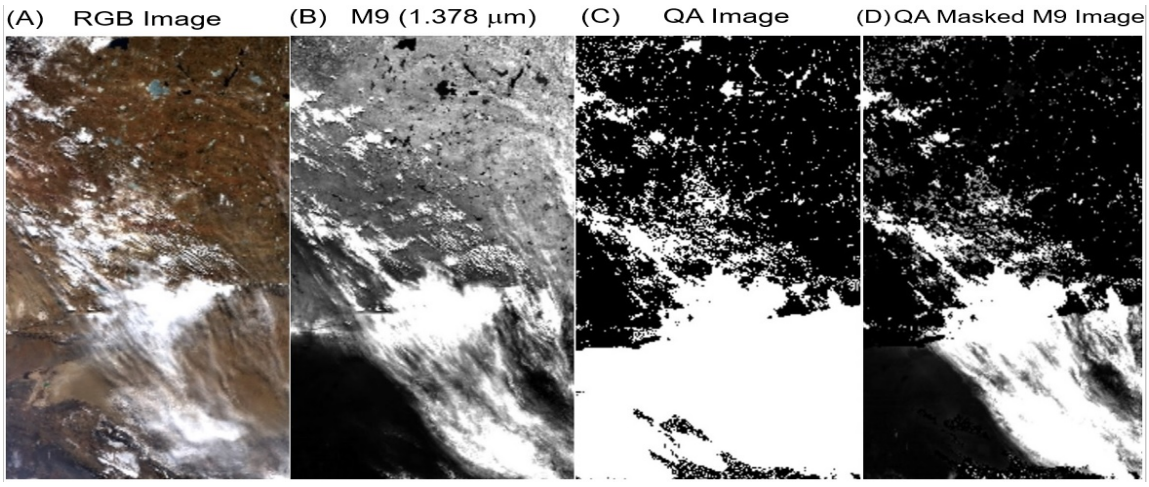

Fig. 18. (A) – A portion of a VIIRS RGB image over Tibet Plateau, (B) – the M9 band apparent reflectance image, (C) – quality assurance (QA) image, and (D) – the QA masked M9 band image.

Through global analysis of VIIRS data acquired in different seasons, we have observed that during dry seasons, over high latitude regions, and over elevated high mountain regions regardless of latitudes, the VIIRS M9 channel is contaminated by reflection from the bottom surfaces. In our implementation of QA routines, we have used different 'threshold' values for different geographical regions. For examples, for regions in the southern hemisphere with latitudes smaller than –60 degrees and with surface elevations greater than 1000 m, if the ratio of the M9 apparent reflectance over the M5 apparent reflectance of a given pixel is less than 0.2, the pixel is assigned a QA value of zero, i.e., the M9 channel of the pixel is affected by reflection from the bottom snow-covered surfaces. For regions in the northern hemisphere with latitudes greater than +60 degrees and with surface elevations greater than 1000 m, if the ratio of the M9 apparent reflectance over the M5 apparent reflectance of a given pixel is less than 0.1, the pixel is assigned a QA value of zero, i.e., the M9 channel of the pixel is affected by reflection from the bottom snow and ice covered surfaces. The reason we selected a

smaller ratio threshold value for the Arctic region is that the Arctic region is generally less dry in comparison with the Antarctic region.

For a pixel within the high elevation Tibet Plateau with latitudes between 27 and +45 degrees, longitudes between 70 and 100 degrees, surface elevation is between 1500 and 3000 m, the apparent reflectance of the M9 channel is less than 0.12, and the apparent reflectance of M8 (1.24 μm) is greater than that of M5 (0.66 μm), the pixel is assigned a QA value of zero. The last requirement, in particular, is essential in assigning the small QA value for the land pixel. However, if the additional test showed that the apparent reflectance of M8 (1.24 μm) is less than 0.08, the QA of the pixel is re-assigned to a value of 2, i.e., the pixel is not a bright land pixel. Also over the Tibet Plateau, but for pixels with surface elevation greater than 3000 m, the M9 channel apparent reflectance threshold is raised to 0.2 (instead of the previous 0.12). The QA routines for the high elevation Andes Mountains and Rocky Mountains are similar to that for the Tibet Plateau, except for minor differences in threshold values. It should be pointed out that our selection of threshold values was made after many tests with multiple VIIRS data sets acquired over different geographical regions and in different seasons! Initially, we also tried to use VIIRS IR emission bands, such as M15 and M16, and to set threshold values for these bands' brightness temperatures for the assignment of QA values, we found that less good consistent results were obtained. Further tests using VIIRS IR emission channels to improve QA parameter assignment are needed in the future.

For polar regions with solar zenith angles greater than 88 degree, we no longer make cirrus reflectance retrievals. The corresponding pixels' cirrus reflectance values are set to zero, and the QA values are also set to zero. For pixels with solar zenith angles less than or equal to 88 degree and with QA value equal to zero (e.g., very dry high elevation mountain pixels such that the M9 band receives small amount of solar radiation reflected by the bottom surfaces), these pixels' cirrus reflectances are re-set to the M9 band's apparent reflectances. *End users of the VIIRS cirrus reflectance products are recommended to mask out these pixels before making quantitative use of the data products.*

3.1.6 Descriptions of input and output data

The VSWIR Level 2 cirrus reflectance algorithm requires input data sets from the standard VSWIR L1b calibrated radiance and geolocation data cubes in netCDF4/HDF5 format. Specifically, the input data for a given VIIRS scene include: number of samples (the data points in the scan direction), number of Lines (the data points in the flight direction), the apparent reflectance of M5 (0.66-μm), M8 (1.24-μm), M9 (1.378-μm), M10 (1.61-μm), and M11 (2.25-μm) channels; the brightness temperature of M14 (8.55-μm),

M15 (10.76-μm), M16 (12.01-μm) channels; Latitude, longitude, surface elevation; solar zenith angle, solar azimuth angle, view zenith angle, and view azimuth angle.

The output data for a given VIIRS scene include: cirrus reflectance for VIS (visible) and NIR (near-IR) channels, cirrus reflectances for SWIR (shortwave IR) channels centered at 1.24, 1.61, and 2.25 μm, and the associated QA (quality assurance) parameter (which is needed for generating the L3 global cirrus reflectance data products from the granule-based L2 data product).

3.1.7 Variance and uncertainty estimates

We have developed an empirical scatter plot approach for the derivation of cirrus reflectances for VIIRS VIS/NIR and SWIR channels. By varying different parameters used in the algorithm, we typically get consistency in the derived slope values (see for examples Fig. 15c and 16c) to within about 2%. Suppose for a thin cirrus pixel with the M9 apparent reflectance value to be 0.025 and the estimated slope value to be 0.5, the estimated cirrus reflectance uncertainty for this pixel would be equal to 0.02x0.025/0.5, which is equal to 0.001. The use of such cirrus reflectance data product in subsequent cirrus corrections would introduce the same amount of error in the derived surface reflectance data product. We feel that our retrieved VIIRS cirrus reflectance data products are suited for use in cirrus corrections, as demonstrated in Fig. 15 and 16. Below we show another excellent example on cirrus detection and correction of VIIRS data for remote sensing of land surfaces and ocean color.

Figure 19a is a portion of a VIIRS RGB image acquired on January 1, 2013 over the Red Sea area. The white cirrus features over land and water surfaces are seen. Fig. 19b is the corresponding M9 (1.378-μm) cirrus image. Here both the land and water surface features are not seen because of strong absorption near 1.378 μm by water vapor beneath cirrus. Fig. 19c is the cirrus removed RGB image. The white cirrus features seen in Fig. 19a disappeared completely in the Fig. 19c image, which indicates the proper removal of thin cirrus scattering effects using the derived cirrus reflectances. In addition, the small greenish-colored water features in the Red Sea of are observed much better than those in the Fig. 19a original RGB image. The small bright cumulus clouds in the upper left portion and lower central portion of the scenes remain in the Fig. 19c image. There are dark features in the Fig. 19c image over desert areas. These features are related to cirrus shadows in the left Fig. 19a RGB image, and they are not results of

over-correction of cirrus effects. They are spatially displaced in comparison with the corresponding cirrus features in Fig. 19b.

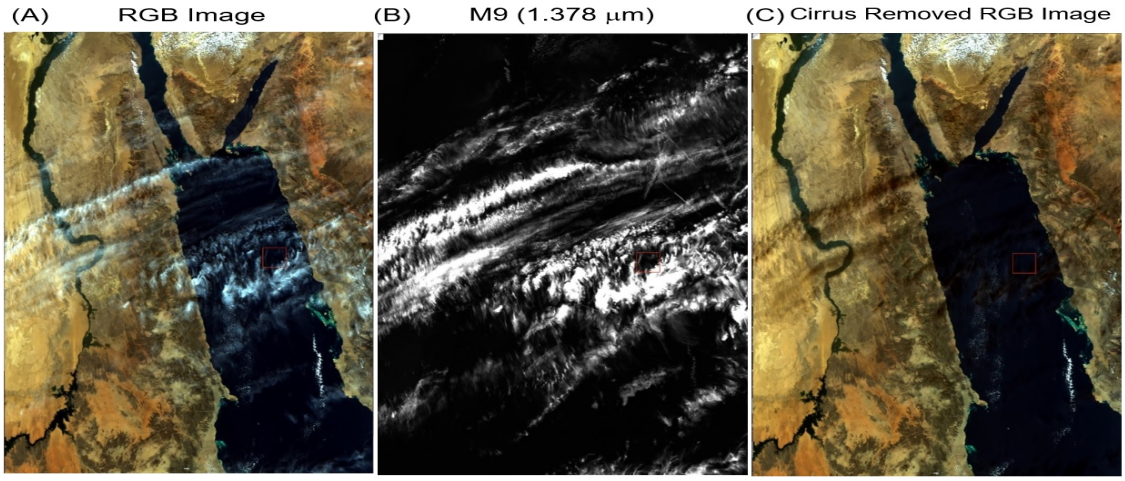

Fig. 19. (A) – A portion of a VIIRS RGB image over Red Sea and nearby areas, (B) – the M9 band apparent reflectance image, and (C) – the cirrus-removed RGB image.

3.2 Practical Considerations

Considerations of numerical computation, programming, and exception handling are presented in this section.

3.2.1 Numerical computation considerations

Problems with numerical stability and round-off errors are not expected with this algorithm.

3.2.2 Programming/procedural considerations

The central portion of the VIIRS cirrus reflectance algorithm is written in Fortran90. This portion of the code is almost machine independent and portable to any computers, as long as a computer has an F90 compiler. The I/O interface to access VIIRS radiance and geolocation data sets in netCDF4/HDF5 and to output the cirrus reflectance data product also in netCDF4/HDF5 files is written in 'c'. The 'c' routines can have minor portability issues with different computers.

4 SAMPLE RESULTS

We have developed a version of netCDF4/HDF5 compatible VIIRS cirrus reflectance algorithm plus a preliminary version of quality assurance (QA) routine on

the University of Wisconsin Atmosphere SIPS computing system. The high quality L2 QA parameters are needed for the subsequent generation of the gridded Level 3 global cirrus reflectance data products on the daily and monthly bases. So far, the algorithm has been tested on the system and made automatic and successful cirrus reflectance retrievals for a few months' of VIIRS data acquired in different seasons. Figure 20 shows sample retrievals of cirrus reflectance images for VIS-NIR channels (M1 - M7), SWIR channels M8 (1.24-μm), M10 (1.61-μm), and M11 (2.25-μm) for one 6-minute VIIRS granule. Excellent cirrus spatial distribution patterns are seen in these images. By comparing Fig. 20c with Fig. 20d, it is seen that the M10 cirrus reflectance values can be smaller than those of the M11. This is because the ice particles within cirrus can have stronger absorption effect over the M10 bandpass than over the M11 bandpass (see also the cirrus spectrum in Fig. 11). Because the VIIRS M10 channel is centered over a spectral region with too much ice absorption over snow and ice covered surfaces, this channel is less useful for quantitative remote sensing of snow and ice surfaces (too dark). It would have been much better if the channel were selected to center at 1.64 μm (the same as MDIS Channel 6) where ice absorption effect is much less.

Fig. 20 Sample retrievals of cirrus reflectances for VIS-NIR channels (M1 - M7), SWIR channels M8 (1.24-μm), M10 (1.61-μm), and M11 (2.25-μm) for one 6-minute VIIRS granule.

5 REFERENCES

Blau, H. H., R. P. Espinola, and E. C. Reifenstein, III, Near infrared scattering by sunlit terrestrial clouds, Applied Opt., 5, 555-454, 1966.

Chen, B., and X. Liu, Seasonal migration of cirrus clouds over the Asian Monsoon regions and the Tibetan Plateau measured from MODIS Terra, Geophys. Res. Lett., 32, L01804, 2005.

Gao, B.-C., A. F. H. Goetz, and W. J. Wiscombe, Cirrus cloud detection from airborne imaging spectrometer data using the 1.38 μm water vapor band, *GRL*., *20*, 301-304, 1993.

Gao, B.-C., and Kaufman, Y. J., Selection of the 1.375-μm MODIS channel for remote sensing of cirrus clouds and stratospheric aerosols from space, *J. Atm. Sci., 52*, 4231-4237, 1995.

Gao, B.-C., et al., Correction of thin cirrus path radiance in the 0.4-1.0 μm spectral region using the sensitive 1.375-μm cirrus detecting channel, *J. Geophys. Res*., 103, 32169-32176, 1998.

Gao, B.-C., Yang, P., Han, W., Li, R.-R., and Wiscombe, W. J., An algorithm using visible and 1.38-◎m channels to retrieve cirrus cloud reflectances from aircraft and satellite data, *IEEE Trans. Geosci. Remote Sensing, 40*, 1659 – 1668, 2002a.

Gao, B.-C., Y. J. Kaufman, D. Tanre, and R.-R. Li, Distinguishing tropospheric aerosols from thin cirrus clouds for improved aerosol retrievals using the ratio of 1.38-◎m and 1.24-◎m channels, Geophys. Res. Lett., 29, 1890, 2002b.

Green, R. O., Eastwood, M. L., Sarture, C. M., et al., Imaging spectrometry and the Airborne Visible/Infrared Imaging Spectrometer (AVIRIS), *Remote Sensing of Environment*, *65*, 227-248, 1998.

Jin, M., MODIS observed seasonal and interannual variations of atmospheric conditions associated with hydrological cycle over Tibetan Plateau, Geophys. Res. Lett., 33, L19707, 2006.

King, M. D., W. P. Menzel, Y. J. Kaufman, D. Tanre, B.-C. Gao, S. Platnick, S. A. Ackerman, L. A. Remer, R. Pincus, and P. A. Hubanks, Cloud and aerosol properties, precipitable water, and profiles of temperature and humidity from MODIS, IEEE Trans. Geosci. Remote Sens., 41, 442-458, 2003.

Murphy, R.E., et al., Update on the algorithmic basis and predicted performance of selected VIIRS environmental data records, ieeexplore.ieee.org/iel5/4087812/4087813/04087886.pdf, 2007.

Salomonson, V. V., Barnes, W. L., Maymon, P. W., Montgomery, H. E., and Ostrow, H., MODIS: Advanced facility instrument for studies of the earth as a system, *IEEE Trans. Geosci. Remote Sens.*, ***27***, 145-153, 1989.

Shiobara, M., and A. Asano, Estimation of cirrus optical thickness from sun photometer measurements, JAM, 33, 672-681, 1994.

Toth, T. D., et al., Investigating enhanced Aqua MODIS aerosol optical depth retrievals over the mid-to-high latitude Southern Oceans through intercomparison with co-located CALIOP, MAN, and AERONET data sets, JGR, 118, 1-15, 2013.

Turk, F. J., S. D. Miller, Toward improved characterization of remotely sensed precipitation regimes with MODIS/AMSR-E blended data techniques, IEEE TGRS, 43, 1059-1069, 2005.

Vane, G., Green, R. O., Chrien, T. G., Enmark, H. T., Hansen, E. G., & Porter, W. M. (1993). The Airborne Visible/Infrared Imaging Spectrometer, *Remote Sensing of the Environment, 44*, 127-143.